Formation and Topology of Foreshock Bubbles

N. Omidi[1], S. H. Lee[2], D. G. Sibeck[2], D. L. Turner[3], T. Z. Liu[4] and V. Angelopoulos[5]

1. Solana Scientific Inc., Solana Beach, CA, USA
2. NASA/GSFC, Greenbelt, MD, USA
3. The Johns Hopkins University Applied Physics Laboratory, MD, USA
4. University Corporation for Atmospheric Research, Geophysical Institute, University of Alaska, Fairbanks, Alaska, USA
5. Department of Earth and Space Sciences, UCLA, Los Angeles, CA, USA

Submitted to Journal of Geophysical Research, 2020

ABSTRACT

We use global and local hybrid (kinetic ions, fluid electrons) simulations to investigate the conditions under which foreshock bubbles (FBs) form and how their topology changes with solar wind conditions. Foreshock bubbles form as a result of the interaction between solar wind discontinuities and backstreaming ion beams in the foreshock. They consist of an outer shock and its associated sheath plasma and a low density high temperature core with low magnetic field strength. The structure of FBs is determined by the angle between the interplanetary magnetic field (IMF) and the normal to the solar wind discontinuity. We show that interaction of rotational discontinuities (RDs) with the foreshock during small angles between the IMF and discontinuity normal results in the formation of a nearly spherical bubble with a radius that scales with the width of the foreshock. As this angle increases FBs become more elongated and eventually become nearly planar structures with dimensions that scale with the length of the foreshock. Despite this transformation, the signatures of FBs in spacecraft time series data remain the same in agreement with the observations. Global simulation results show that FBs form when the solar wind flow speed corresponds to high or intermediate Alfvén Mach numbers (~>7 M_A). In general, this is tied to the relative speed between the solar wind and ion beams and drop in density of the backstreaming ions.

1. INTRODUCTION

Collisionless ion dissipation processes at the bow shock lead to the formation of the foreshock, a region upstream of the quasi-parallel bow shock populated with backstreaming ion beams, ULF waves and nonlinear structures which have been the topics of extensive studies at Earth [e.g. *Asbridge et al., 1968; Greenstadt et al., 1968; 1980; Gosling et al., 1978; Paschmann et al., 1979; Bonifazi, Egidi, et al., 1980; Bonifazi, Moreno, et al., 1980; Hoppe et al., 1981; Russell and Hoppe 1983; Le and Russell, 1992; Omidi 2007; Blanco-Cano et al., 2009, 2011; Kajdic et al. 2010, 2011, 2013; Sibeck et al., 2008; Omidi et al., 2009; Omidi, Sibeck, et al., 2013; Omidi, Zhang, et al., 2013; 2014; Rojas-Castillo et al., 2013; Zhang et al., 2013*].

Using global and local electromagnetic hybrid (kinetic ions, fluid electrons) simulations, *Omidi et al., [2010]* showed that the interaction between rotational discontinuities (RDs) embedded in the solar wind and the backstreaming ion beams in the foreshock results in the formation of nonlinear structures named foreshock bubbles (FB). The interaction initially results in the deflection and deceleration of the solar wind and the reflection of a fraction of the ion beam, followed by the launch of a sunward propagating fast magnetosonic shock. Downstream of this shock is a decelerated and heated sheath plasma which surrounds an inner core exhibiting hot and tenuous populations of ions and electrons. The core magnetic field strength is typically depressed with ULF waves superposed. Although the shock wave associated with the foreshock bubble propagates sunward in the solar wind frame, the structure as a whole is carried by the solar wind in the anti-sunward direction. As a result, under condition of small and intermediate IMF cone angles prior to the arrival of the RD, the resultant FBs are carried towards the bow shock and ultimately collide with it and the dayside magnetosphere resulting in global magnetospheric impacts. In addition, the motion of the foreshock bubble towards the bow shock constitutes a unique opportunity for particle acceleration through Fermi processes making them an efficient means of particle energization.

Observational confirmation for the existence of foreshock bubbles was first provided by *Turner et al. [2013]* who used multi-spacecraft THEMIS observations to demonstrate the formation and the evolution of foreshock bubbles. They established the criteria necessary for distinguishing between FBs and hot flow anomalies (HFAs) that form as a result of the interaction between solar wind discontinuities and the bow shock [e.g. *Schwartz, 1995; Schwartz et al., 1988, 2000; Thomsen et al., 1986, 1988, 1993; Paschmann et al., 1988; Burgess, 1989; Thomas et al., 1991; Sibeck et al., 1998, 1999, 2000; Lin, 1997, 2002; Lucek et al., 2004; Omidi and Sibeck, 2007; Facsko et al., 2008; Eastwood et al., 2008; Jacobsen et al., 2009; Zhang et al. 2010*]. Although FBs and HFAs have distinctly different sizes and structures, their signatures in spacecraft time series data have many similarities requiring proper attention to distinguish between the two. *Turner et al. [2013]* demonstrated that the size of foreshock bubbles at Earth is ~10 R_E, confirming the predictions by *Omidi et al. [2010]*. In contrast, HFAs are smaller at about 1-2 R_E. Observations confirm that the core region of foreshock bubbles contains high energy particles.

Subsequent investigations of foreshock bubbles have revealed additional information regarding their properties, formation and impacts on the magnetosphere. For example, *Hartinger et al. [2013]* showed the excitation of Pc5 ULF waves in the magnetosphere in response to foreshock bubbles colliding with the bow shock and impacting magnetosheath plasma and the magnetopause. Similarly, using data from spacecraft located in the foreshock and magnetosphere and ground based observations, *Archer et al. [2015]* demonstrated that foreshock bubbles have a global impact on the magnetosphere-ionosphere system as suggested in *Omidi et al. [2010]*. They also showed that amongst the various foreshock transients, FBs have the largest impact on the magnetosphere and ionosphere. *Omidi et al. [2010]* demonstrated the formation of foreshock bubbles by rotational discontinuities in the solar wind. Subsequently, *Liu et al. [2015]* showed the formation of FBs by tangential discontinuities (TDs) using THEMIS data. They showed that this occurs due to the finite size of the superthermal upstream ion gyrodadii that can penetrate through the thin discontinuity boundary. While the finite size of the solar wind discontinuity makes its nature (TD versus RD) less important for FB generation, the fact that TDs (with no normal component of magnetic field) can generate FBs suggests that there is a wide range of normals that can result in FBs, a situation that has not been previously explored, and requires further study by observations and simulations. *Liu, Hietela, et al. [2016]* used multipoint observations of foreshock bubbles to examine their structure and evolution and show how they compare to hot flow anomalies. Using the properties of 6 observed FBs, they showed their sizes to vary between 2 and 15 R_E. *Liu, Turner, et al. [2016]* showed that in agreement with the results of hybrid simulations, the quasi-parallel portion of the shock wave associated with the FBs is responsible for the formation of a new foreshock upstream of it. As the FB collides with the bow shock, the old bow shock dissipates and is replaced with the FB shock wave and the associated foreshock. *Liu, Angelopoulos, et al. [2017]; Liu, Lu, et al. [2017]; Liu, Lu, et al. [2018]* have examined ion and electron acceleration by foreshock bubbles further establishing them as efficient particle accelerators via Fermi processes. Acceleration of electrons to relativistic energies by foreshock bubbles has been investigated by *Wilson et al. [2016]* providing further evidence for their significant role in particle energization. *Turner et al. [2020]* analyzed MMS observations of foreshock bubbles and reported observations of deep localized magnetic holes within the FB core region. *Sun et al. [2020]* compared the properties of FBs observed by MMS spacecraft with those predicted by hybrid simulations. Finally, *Omidi et al. [2020]* used 3-D hybrid simulations and Venus Express data to demonstrate that despite the smaller size of the Venusian foreshock, FBs can also form at Venus resulting in major ionospheric impacts including its sunward expansion and escape of ionospheric O^+ ions.

In this paper, we use 2.5-D global and local hybrid simulations to improve our understanding of formation and topology of foreshock bubbles. Specifically, in Section 2 we examine the generation and topological variations of foreshock bubbles expected as a function of the angle between the interplanetary magnetic field (IMF) and the discontinuity normal. Section 3 examines the Mach number dependency of foreshock bubbles and how their formation depends on ion beam speed and density. Section 4 provides summary and conclusions.

2. TOPOLOGY OF FORESHOCK BUBBLES

The parameter which has the biggest influence on the topology and structure of foreshock bubbles is the angle between the IMF and the discontinuity normal vector (**n**). Here we use simple diagrams in Figure 1 to illustrate this point. Panel 1a presents the configuration for radial IMF where the cone angle between the IMF and flow velocity is 0^o, the discontinuity normal is along the IMF, and the discontinuity is an RD. This geometry is similar to that considered by *Omidi et al. [2010]* who showed that a nearly spherical bubble formed with a size that scales with the width of the foreshock. Panel 1b also presents a situation where (**n**) is again parallel to the IMF but the cone angle is 90^o and the foreshock lies on the flanks (or high latitudes) of the bow shock. As in Panel 1a, this configuration also results in the formation of a nearly spherical foreshock bubble with a size that scales with the width of the foreshock. Panels 1c and 1d correspond to a configuration where the IMF and (**n)** are perpendicular (here the discontinuity is a TD) with 1c representing a radial IMF and 1d a cone angle of 90^o. This geometry is similar to that discussed by *Liu et al. [2015]*. In this limit-case, the TD encounters the foreshock along the full length of it as opposed to its width. As such, the size of the FB scales with the length of the foreshock as opposed to its width. This also implies that the FB cannot be spherical but as the angle between (**n**) and IMF progressively increases it must instead assume a more planar structure.

Figure 1 depicts limit-cases to illustrate why we expect the topology of foreshock bubbles to change with the angle between IMF and (**n**). In the remainder of this section we use the results of 2.5-D global hybrid simulations to investigate how the structure of FBs changes with this angle. We note that 3-D global hybrid simulations of foreshock bubbles result in structures very similar to those obtained from 2.5-D runs *Omidi et al. [2020]*. The simulation model used for the global runs is similar to that in *Omidi et al. [2009]* where a plasma reflecting obstacle is used to generate the bow shock and the associated foreshock. Simulations are performed in the X-Y plane with the solar wind injected continuously from the X = 0 boundary and flow speed that in general may be in the X-Y plane. A number of different box sizes are used to accommodate changes in FB topology with solar wind conditions. Also, the proton skin depth (c/ω_p) is used to specify the size of the simulation box where c is the speed of light and ω_p is the proton plasma frequency. As noted below, different solar wind flow speeds are used in the study. However, in all cases electron and ion betas (ratio of thermal to magnetic pressure) are set to 0.5 and 1 respectively.

Figure 2 shows results from a global hybrid run with IMF and flow speed along the X direction and solar wind Alfvén Mach $M_A = 15$. Panel 2a shows density normalized to solar wind value and magnetic field lines; Panel 2b shows total magnetic field strength normalized to IMF strength and the position of the RD responsible for FB formation; 2c shows ion temperature normalized to solar wind value and Panel 2d corresponds to flow speed normalized to upstream Alfvén speed (V_A). We note that the presence of the RD results in a change in the cone angle to 26^o by introducing a Z component of the magnetic field behind the discontinuity which implies an increase in total magnetic field strength. While MHD Rankine-Hugoniot conditions imply no change in magnetic field strength across an RD, in kinetic plasmas this condition is not typically satisfied, e.g. the magnetopause during southward IMF. Figure 2a identifies the foreshock bubble and the associated shock, sheath and the core formed in this run as well as the new foreshock formed upstream of the FB. Figure 2b shows the magnetic signatures of the FB which due to the fast magnetosonic nature of the shock correlates with density at the shock and in the sheath. The core region is associated with a turbulent magnetic field strength due to ULF waves generated in the foreshock. Figure 2c shows elevated temperatures in the foreshock due to the presence of backstreaming ion beams, however, the core region of the FB is associated with higher temperatures (more energetic ions). Figure 2d shows lowering of the flow speed in the foreshock and deceleration within the core of the foreshock bubble. Figures 2a, 2b also show the enhancement in density and magnetic field associated with the foreshock compressional boundary (FCB) [*Sibeck et al., 2008; Omidi et al., 2009; Omidi, Sibeck et al., 2013; Rojas-Castillo et al., 2013*]. It is evident in Figure 2 that the size of the foreshock bubble transverse to the Sun-Earth line is comparable to the width of the foreshock.

Figure 3 is similar to Figure 2 except that it corresponds to a run with IMF cone angle of 15^{o} prior to the arrival of the RD in which the Y (tangential) component of the magnetic field reverses sign. This rotation is clear in Figure 3a which shows 3 magnetic field lines. The general features of the foreshock bubble in Figure 3 are similar to those in Figure 2, i.e. the presence of a shock, sheath and a core associated with reduced density, velocity and enhanced temperature. The presence of ULF waves and turbulence in the core is also similar to that observed in Figure 2. However, the size of the FB formed in

Figure 3 is larger in the Y direction by virtue of the fact that the width of the foreshock (in the Y direction) is larger as compared to the radial IMF case.

Figure 4 shows results from a run with IMF cone angle of 30^o before the arrival of the RD which rotates the Y component of the magnetic field by 180^o. As in the previous runs, the general plasma and magnetic field properties of the resulting FB exhibits a shock, sheath and a core with features similar to those seen in Figures 2 and 3. On the other hand, the size of the FB in Figure 4 increases further in the Y direction due to the even broader width of the foreshock and the extension of the quasi-parallel bow shock to the flank (or higher latitudes) of the bow shock surface. Comparison of Figures 2, 3 and 4 shows clear evidence for the elongation of the foreshock bubble in the Y direction with increasing IMF cone angle, which demonstrates its topological evolution.

Further increases in the IMF cone angle and the movement of the ion foreshock towards the flanks (or higher latitudes) result in a further elongation of the FB in the Y direction and a topology approaching a planar structure. Figure 5 presents results for the cone angle of 60^o with (**n**) along the X direction as in the previous runs. It shows the formation of a planar FB that extends from the bow shock all the way to the Y = 0 boundary of the simulation box. In reality, such FBs may extend 10s of R_E perpendicular to the flank given that the quasi-parallel bow shock and the associated foreshock may extend more than 100 R_E down the tail. The strength of the FB decreases with distance from the bow shock. Despite the large IMF cone angle the FB continues to exhibit a structure consisting of a shock, sheath and a core, albeit now much more planar in nature. As such, the passage of this planar FB over a spacecraft produces a similar time series data. This is demonstrated in panels e-h in Figure 5 that show the ion temperature, flow velocity in X, density and magnetic field strength as a function of time as observed by the simulated spacecraft marked by “S” in Figure 5b. The resulting time series data shows the classic features of an FB with the spacecraft first encountering the core region, followed by the sheath plasma and the shock wave. An interesting aspect of planar FBs is that their shock and the bow shock combine into in a single deformed bow shock similar to what happens at the Titan-Saturn system during periods of high solar wind pressure [*Omidi et al., 2017*]. Under these conditions, ions escaping the quasi-parallel bow shock can interact with the quasi-perpendicular portions of the bow shock resulting in further acceleration through shock drift processes. Figure 6a shows the ion temperature from the run with cone angle of 60^o zoomed near the FB and the quasi-perpendicular portion of the bow shock. Also shown are two magnetic field lines serving to locate the RD and demonstrate the magnetic connection from the FB shock wave to the bow shock. It is evident from Figure 6a that some ions can escape the FB bow shock and follow the magnetic field to regions close to the quasi-perpendicular bow shock despite the FB’s shock normal angle being 60^o.

Figures 6b and 6c show the density and temperature from a run with an IMF cone angle of 89^o and M_A = 15. A number of magnetic field lines are also shown in both panels which serve to locate the position of the RD. Again, the Y component of the magnetic field (in this case the predominant component) rotates by 180^o. It is evident from these panels that no foreshock bubble has formed in this run. The reason is evident in Figure 6c which shows that the backstreaming ion beams originating at the quasi-parallel shock are accelerated tailwards (+X direction) by the motional electric field in the solar wind as they move in the –Y direction. This implies that the relative speed between the solar wind discontinuity and ion beams is reduced; as demonstrated in the next section this has a major effect on FB formation. The results in Figure 6b illustrate that as the IMF cone angle increases and the motional electric field pushes the backstreaming ion beams tailward the processes of FB formation comes to a halt. It implies that while RDs near the limit of TDs (i.e. a small normal component of magnetic field) can still result in the formation of foreshock bubbles, TDs themselves may or may not lead to the generation of FBs depending on the solar wind conditions.

The planar foreshock bubble in Figure 5 corresponds to a configuration similar to that depicted in Figure 1d, although it does not correspond to the TD limit. In the remainder of this section we show results from a run that is similar to the configuration in Figure 1c, but includes an RD instead of a TD. Figure 7 shows the density from this run at 4 different times corresponding to 75 to 175 Ω^{-1} where Ω is the proton gyro-frequency. Also shown in red are magnetic field lines and in white dashed lines showing the RD which has a normal (**n**) along the Y direction. Figure 7a shows the solar wind flow vector (V_{SW}) which has a component of 15 V_A along the X direction and 2 V_A along the Y direction so that the RD moves in the +Y direction. Figure 7a corresponds to a time when the RD has just encountered the foreshock. By the time corresponding to Figure 7b, the RD has moved further into the foreshock and as a result a planar FB has formed extending from the bow shock sunward into the foreshock. Figure 7c depicts a time when the RD intersection with the bow shock results in the formation of a hot flow anomaly which does not extend as far away from the bow shock as the FB. As the RD continues to traverse the foreshock it eventually reaches locations that fall outside of the preexisting foreshock and as a result the FB dissipates. Figure 7d corresponds to such a time when the RD is nearly out of the foreshock and the foreshock bubble is no longer present. In contrast, the HFA continues to exist at the intersection of the RD with the bow shock due to the interaction of the reflected ions with the RD there. When the RD passes beyond the bow shock, the HFA will also dissipate. The interpretation that both a foreshock bubble and an HFA are formed in this run is consistent with the fact that the FB forms prior to the formation of the HFA, they co-exist for some time and then the FB dissipates while the HFA is still active. Similarly, although not shown here both the FB and the HFA in Figure 7 exhibit all the expected plasma and magnetic signatures and the distinctions discussed by *Turner et al. [2013]*.

3. MACH NUMBER DEPENDENCE OF FORESHOCK BUBBLES

In this section, we use global and local hybrid simulations to investigate the dependence of foreshock bubble formation on solar wind speed and the density of the backstreaming ions. Figure 8a, b, c show the density normalized to solar wind value from three runs with the IMF and discontinuity normal (**n**) along the X direction and solar wind Alfvén Mach numbers of 15, 11 and 7 respectively. It is evident from this figure that the density jump associated with the FB shock and sheath diminish with decreasing Mach number indicating the weakening of the FB. This suggests that foreshock bubbles only form at intermediate and high solar wind Mach numbers. To further substantiate this conclusion, Figure 9 shows the density from three runs with RD normal along X and IMF cone angle of 60^o with panels a, b and c corresponding to solar wind Mach numbers of 15, 11 and 7 respectively. As in the case of spherical FBs, Figure 9 illustrates that the density perturbations associated with the planar FBs also diminish with decreasing Mach. Note that in the case of Figure 9c, the foreshock bubble is not strong enough to extend all the way to the Y = 0 boundary of the simulation box.

The weakening of the foreshock bubbles with reduced solar wind Mach number could be due to two factors: First there is a reduction in the relative velocity between the solar wind and backstreaming ion beams in the foreshock. Second, there is a decrease in the densities of the backstreaming ion beams as a result of the reduced shock strength. In order to better understand the role of each of these factors, we use local hybrid simulations first employed by *Omidi et al. [2010]* to generate foreshock bubbles. In this approach the bow shock is replaced by a finite width (in Y direction) ion beam injected continuously from the right hand boundary of the simulation box with a beam velocity in the –X (sunward) direction, while the solar wind and the embedded RD is injected from the left hand boundary as usual with a velocity along the X direction. The advantage of this approach lies with the fact that we have direct control over the density and velocity of the backstreaming ion beams independent of solar wind conditions allowing us to better understand the role of each parameter in FB formation. In all the local hybrid runs discussed below we assume both the IMF and the RD normal are in the X direction.

Figure 10 shows the density normalized to its upstream value from four local hybrid runs. In all four runs, the density of the backstreaming ion beams is set at 5% of the solar wind density. The velocity of the backstreaming ion beams is set to that of the solar wind which corresponds to M_A = 11, 9, 8 and 7 in Figures 10a, b, c, d respectively. Also shown in each panel is the simulation time which increases with decreasing Mach number. It is evident in Figure 10 that despite the beam density being the same in all four runs, the strength of the resulting FBs decreases with decreasing Mach number. Accordingly, the observed reduction in the strength of the FBs in global simulations with Mach number is directly tied to the decrease in the relative speed between the solar wind and the backstreaming ions.

While the relative speed between the solar wind and the backstreaming ions plays a critical role in the formation of foreshock bubbles, the density of these ions also plays a critical role as demonstrated below. Figure 11 shows the density from four runs in which the solar wind and ion beam velocity is 11 V_A in +X and –X respectively while the beam density corresponds to 5% of solar wind in Figure 11a, 2.5% in 11b, 1% in 11c and 0.5% in 11d. It is evident that when the beam density is 1% of solar wind or more a foreshock bubble forms, while for density of 0.5% no FB forms although density structures associated with the generation of ULF waves are evident in panel 11d. In the following, we further discuss the role of ion beam density in the formation of foreshock bubbles.

To examine the interaction between the ion beam and RD in some detail, we compare results from the two runs corresponding to beam densities of 0.5% and 5% in Figure 11.

Specifically, we examine the evolution of the RD using the Z component of the magnetic field (B_Z) and the backstreaming ions using temperature. Panel a in Figure 12 shows the profile of B_Z as a function of X (at Y = 150) and the total temperature as a function of X and Y at time 5.12 Ω^{-1} for the run with beam density of 0.5%. The RD is identified by the red dashed line with $B_Z = 0$ to the right of it and $B_Z = 0.5$ (normalized to IMF strength) to the left. Ion temperature allows us to identify the ion beam and examine its evolution despite its low density because its presence elevates the second moment of the distribution function and temperature. Note that for the sake of clarity, the limits on the temperature color bar are not the true maximum values. Figure 12a corresponds to the time of initial interaction between the ion beam and the RD with little change in either. Figure 12b corresponds to a later time when the RD has moved further to the right and the ion beam to the left. The overall structure of the RD remains unchanged. Figure 13c depicts the system at time 25 Ω^{-1} which shows large amplitude oscillations associated with the excitation of ULF waves to the left of the RD. These waves are generated by the interaction of the backstreaming ions and the solar wind with their wave vector pointing in the –X (sunward) direction, however, they are carried in the +X direction by the solar wind. This can be seen in Figure 13d which shows further evolution of the waves. It is also evident that the RD remains relatively unchanged and that the ion beam goes through the discontinuity without significant interaction.

Figure 13 is similar to Figure 12 except that it corresponds to the run with beam density of 5%. One difference between the two figures is that due to the larger density of the ion beam, ULF waves are excited earlier and they can be seen both upstream and downstream of the RD. For our purposes, a more dramatic difference is the nature of the interaction between the RD and the ion beam. For example, a comparison between Figures 13b and 13c shows a marked increase in the amplitude of the RD and steepening of the discontinuity front. Figure 13d shows further growth and steepening of the RD which results in the reflection of a fraction of the ion beam and the formation of the foreshock bubble. The results demonstrate that the formation of foreshock bubbles is tied to a nonlinear coupling between the RD and the backstreaming ion beam which results in amplification and steepening of the RD and reflection of a portion of the beam. This interaction occurs for beam densities of ~>1% of solar wind density.

4. SUMMARY AND CONCLUSIONS

We have used the results of global and local 2.5-D hybrid (kinetic ions, fluid electrons) simulations to investigate and understand the formation and topology of foreshock bubbles. In regards to topology, the most influential parameter is the angle between the IMF and the discontinuity normal. By performing four global simulations with discontinuity normals along the X direction and IMF cone angles of 0^o, 15^o, 30^o, 60^o we demonstrate the topological transformation of FBs from spherical to planar structures. A change in the direction of the IMF from cone angle of 0^o to 15^o results in an elongation of the FB which occurs due to the broadening of the foreshock. Further increase to cone angle of 30^o leads to even more pronounced elongation of the FB as the quasi-parallel shock and the foreshock move towards the flanks (or higher latitudes). With a cone angle of 60^o, a planar FB forms on the flanks or high latitudes which may extend 10s of R_E

away from the bow shock. An interesting aspect of this geometry is the possibility of energetic ions escaping from the foreshock bubble and then interacting with the quasi-perpendicular bow shock, undergoing further acceleration through shock drift acceleration.

Global hybrid simulations at larger cone angles (89^{o} in this study) show that the interaction between the discontinuity and the foreshock does not result in the formation of a foreshock bubble. The reason for this is the presence of the motional electric field in the solar wind which results in the tailward acceleration of the ion beams originating at the quasi-parallel bow shock as they move upstream. As a result, the relative speed between the discontinuity and the ion beams is reduced which inhibits the formation of a foreshock bubble. In general, as RDs approach the TD limit (i.e. a small normal component of the magnetic field) the presence of the motional electric field in the solar wind results in the reduction of the relative speed between the discontinuity and the ion beams which limits but does not prohibit the formation of a FB.

We also used a global hybrid simulation to demonstrate the formation of planar foreshock bubbles during periods of small IMF cone angle with discontinuity normals at large angles with respect to the IMF. A distinction between this case and that for planar FBs during large IMF cone angles is the width of the foreshock. During small cone angles the width of the foreshock is ~10 R_E vs. ~100 R_E during large IMF cone angles. As such, the distance traveled by the FB before dissipation is smaller during small IMF cone angles. The results also showed the formation of a hot flow anomaly due to the intersection of the RD with the bow shock demonstrating that one discontinuity can result in the formation of both a foreshock bubble and a HFA. This was also demonstrated in 3-D hybrid simulation results reported by *Omidi et al. [2020]*.

Using results from global hybrid simulations, we showed that both spherical and planar foreshock bubbles become weaker as the solar wind Mach number decreases. FBs are expected to form for intermediate and high Alfvén Mach numbers M_A ~> 7. This is in agreement with the observations reported by *Turner et al. [2020]* and *Lee et al. [2020]*. To further understand the role of the relative speed between the solar wind and the ion beam as well as the density of the backstreaming ions we performed local hybrid simulations in which the bow shock is replaced with a beam of ions with finite width. The results show that keeping the density of the ion beam at 5% of the solar wind density and reducing the solar wind speed results in weakening of the foreshock bubble, indicating the importance of the flow speed in FB formation. Using four runs with solar wind flow speed of $M_A = 11$ and ion beam densities of 5%, 2.5%, 1% and 0.5% we showed the weakening of the FBs with reduced beam densities such that no FB is formed when beam density of 0.5% is used. Comparing the properties of the RDs and ion beams in the runs with beam densities of 5% and 0.5% shows considerable differences between the two. Specifically, with beam density of 0.5% the RD is found to remain unchanged as the ion beam passes through it without any reflection. When beam density of 5% is used the RD is found to grow in amplitude and steepen as it encounters the beam. This steepening also results in the reflection of a fraction of the ion beam. The results demonstrate that the formation of foreshock bubbles is tied to a nonlinear interaction between the RD and the ion beam. The role of FB topology on ion acceleration processes is an important question currently under investigation and will be discussed in a future publication.

AKNOWLEDGMENTS

Work for this project was supported by NASA grant #80NSCC18K1036 to Solana Scientific Inc. and NASA RTOP "Formation and Properties of Foreshock Bubbles" support for S. H. Lee and D. G. Sibeck. D. Turner acknowledges MMS contract NNG04EB99C at Southwest Research Institute. V.A. acknowledges support from NASA NAS5-02099. Simulation data is available at http://solanascientific.org .

REFERENCES

Archer, M. O., D. L. Turner, J. P. Eastwood, S. J. Schwartz, and T. S. Horbury (2015), Global impacts of a foreshock bubble: Magnetosheath, magnetopause and ground-based observations, Planet. Space Sci., 106, 56–65, doi:10.1016/j.pss.2014.11.026.

Asbridge, J. R., S. J. Bame, and I.B. Strong (1968), Outward flow of protons from the earth's bow shock, *J. Geophys. Res.*, 73, 5777.

Blanco-Cano, X., N. Omidi and C.T. Russell (2009), Global hybrid simulations: Foreshock waves and cavitons under radial IMF geometry, *J. Geophys. Res.*, 114, A01216, doi:10.1029/2008JA013406.

Blanco-Cano, X., P. Kajdič, N. Omidi, and C. T. Russell (2011), Foreshock cavitons for different interplanetary magnetic field geometries: Simulations and observations, J. Geophys. Res., 116, A09101, doi:10.1029/2010JA016413.

Bonifazi, C., A. Egidi, G. Moreno, and S. Orsini (1980a), Backstreaming ions outside the earth's bow shock and their interaction with the solar wind, *J. Geophys. Res.*, 85, 3461.

Bonifazi, C., G. Moreno, A. J. Lazarus, and J. D. Sullivan (1980b), Deceleration of the solar wind in the earth's foreshock region: ISEE 2 and IMP 8 observations, *J. Geophys. Res.*, 85, 6031.

Burgess, D. (1989), On the effect of a tangential discontinuity on ions specularly reflected at an oblique shock, *J. Geophys. Res.*, 94, 472.

Eastwood, J. P., et al. (2008), Themis observations of a hot flow anomaly: Solar wind, magnetosheath, and ground-based measurements, Geophys. Res. Lett., 35, 332 doi:10.1029/2008GL033475.

Facsko, G., K. Kecskemety, G. Erdos, M. Tatrallyay, P. W. Daly, and I. Dandouras (2008), A statistical study of hot ow anomalies using Cluster data, Advances in space research, 41 (8), 1286, doi:10.1016/j.asr.2008.02.005.

Gosling J. T., J.R. Asbridge, S. J. Bame, G. Paschmann, and N. Sckopke (1978), Observations of two distinct populations of bow shock ions in the upstream solar wind, *J. Geophys. Res*, 5, 957.

Greenstadt , E.W., et al. (1968), Strong, correlated magnetic field and plasma observations of the Earth's bow shock, *J. Geophys. Res*, 73, 51.

Greenstadt, E.W., C.T. Russell, and M. Hoppe (1980), Magnetic field orientation and suprathermal ion streams in the earth's foreshock, *J. Geophys. Res*, 85, 3473.

Hoppe, M. M., C. T. Russell, L. A. Frank, T. E. Eastman, and E. W. Greenstadt (1981), Upstream hydromagnetic waves and their association with backstreaming ion populations: ISEE-1 and -2 observations, J. Geophys. Res., 86, 4471–4492, doi:10.1029/JA086iA06p04471.

Jacobsen, K.S., et al. (2009), THEMIS observations of extreme magnetopause motion caused by a hot flow anomaly, *J.Geophys.Res.*, 114, doi:10.1029/2008JA013873.

Kajdič, P., X. Blanco-Cano, N. Omidi, and C. T. Russell (2010), Analysis of waves surrounding the foreshock cavitons, AIP Conf. Proc., 1216, 479–482, doi:10.1063/1.3395907.

Kajdič, P., X. Blanco-Cano, N. Omidi, and C. T. Russell (2011), Multispacecraft study of foreshock cavitons, Planet. Space Sci., 59, 705–714, doi:10.1016/j.pss.2011. 02.005.

Kajdič, P., X. Blanco-Cano2, N. Omidi, K. Meziane, and C. T. Russell (2013), Statistical study of foreshock cavitons, Ann. Geophys., 31, 2163–2178, doi:10.5194/angeo-31-2163-2013.

Le, G. and C.T. Russell (1992), A study of ULF wave foreshock morphology, II: Spatial variations of ULF waves, *Planet. Space Sci.*, 40.

Lee S. H., D. G. Sibeck, N. Omidi, M. V. D. Silveira, B. L. Giles, R. B., Torbert, C. T. Russell, H. Wei, J. L. Burch (2020), Comparison of MMS Observations of Foreshock Bubbles with the Global Hybrid Simulation, *J. Geophys. Res.*, submitted.

Lin, Y. (1997), Generation of anomalous flows near the bow shock by its interaction with interplanetary discontinuities, *J. Geophys. Res.*, 102, 24265.

Lin, Y. (2002), Global hybrid simulation of hot flow anomalies near the bow shock and in the magnetosheath, Planetary and space science, 50 (5-6), 577, Symposium on Intercomparative Magnetosheath Studies, ANTALYA, TURKEY, SEP 04-08, 2000.

Liu, Z., D. L. Turner, V. Angelopoulos, and N. Omidi (2015), THEMIS observations of tangential discontinuity-driven foreshock bubbles, *Geophys. Res. Lett*., 42, doi:10.1002/2015GL065842.

Liu, T. Z., H. Hietala, V. Angelopoulos, and D. L. Turner (2016), Observations of a new foreshock region upstream of a foreshock bubble’s shock, Geophys. Res. Lett., 43, 4708–4715, doi:10.1002/2016GL068984.

Liu, T. Z., D. Turner, et al. (2016), Multipoint observations of the structure and evolution of foreshock bubbles and their relation to hot flow anomalies, *J. Geophys. Res., 121,* doi:10.002/2016JA022461.

Liu, T. Z., V. Angelopoulos, et al. (2017), Statistical study of particle acceleration in the core of foreshock transients, *J. Geophys. Res.*, *122*, 7197-7208, doi:10.1002/2017JA024043.

Liu, T. Z., S. Lu, et al. (2017), Fermi acceleration of electrons inside foreshock transient cores, *J. Geophys. Res., 122*, 9248-9263, doi:*10.1002/2017JA024480*.

Liu, T. Z., Lu, S., Angelopoulos, V., Lin, Y., & Wang, X. Y. (2018). Ion acceleration inside foreshock transients. *Journal of Geophysical Research: Space Physics, 123*, 163–178. https://doi.org/10.1002/ 2017JA024838.

Lucek, E. A., et al. (2004), Cluster observations of hot flow anomalies, , *J. Geophys. Res.*, 109, A06207,doi:10.1029/2003JA010016.

Omidi, N. (2007), Formation of foreshock cavities, in *Turbulence and Nonlinear Processes in Astrophysical Plasmas* , Editors D. Shaikh and G. Zank, AIP Conference Proceedings, 932, 181.

Omidi, N., and D. Sibeck (2007), Formation of hot flow anomalies and solitary shocks, *J. Geophys. Res.*, 112, A01203, doi:10.1029/2006JA011663.

Omidi, N., D. Sibeck, and X. Blanco-Cano (2009), The foreshock compressional boundary, J. Geophys. Res., 114, A08205, doi:10.1029/2008JA013950.

Omidi, N., J. Eastwood and D. Sibeck (2010), Foreshock bubbles and their global magnetospheric impacts, *J. Geophys.Res.*, 115, A06204, doi:10.1029/2009JA014828.

Omidi, N., D. Sibeck, X. Blanco-Cano, D. Rojas-Castillo, D. Turner, H. Zhang, and P. Kajdi_c (2013), Dynamics of the foreshock compressional boundary and its connection to foreshock cavities, J. Geophys. Res. Space Physics, 118, 823–831, doi:10.1002/jgra.50146.

Omidi, N., H. Zhang, D. Sibeck and D. Turner (2013), Spontaneous hot flow anomalies at quasi-parallel shocks: 2. Hybrid simulations, *J. Geophys.Res.*, 118, 173–180, doi: 10.1029/2012JA018099.

Omidi, N., Sulaiman, A. H., Kurth, W., Madanian, H., Cravens, T., Sergis, N., Edberg, N. J. T. (2017). A single deformed bow shock for Titan-Saturn system. Journal of Geophysical Research: Space Physics, 122. https://doi.org/10.1002/2017JA024672

Omidi, N., Collinson, G., & Sibeck, D. (2020). Foreshock bubbles at Venus: Hybrid simulations and VEX observations. *Journal of Geophysical Research: Space Physics*, **125**, e2019JA027056. https://doi.org/10.1029/2019JA027056

Paschmann et al. (1979), Association of low frequency waves with suprathermal ions in the upstream solar wind, *Geophys.Res.Lett.*, 6, 209.

Paschmann, G., et al. (1988), 3-Dimensional plasma structures with anomalous flow directions near the Earth's bow shock, *J. Geophys. Res.*, 93,11279.

Rojas-Castillo, D., X. Blanco-Cano, P. Kajdi_c, and N. Omidi (2013), Foreshock compressional boundaries observed by Cluster, J. Geophys. Res. Space Physics, 118, 698–715, doi:10.1029/2011JA017385.

Russell, C.T. and M. Hoppe (1983), Upstream waves and particles, *Space Sci Revs*, 34, 155.

Schwartz, S. J., et al. (1988), An active current sheet near the earth's bow shock, *J. Geophys. Res.*, 93,11295.

Schwartz, S. J. (1995), Hot flow anomalies near the earth's bow shock, in *Physics of Collisionless Shocks*, C.T. Russell Editor, Advances in Space Research, Pergamon, 107.

Schwartz, S. J., et al. (2000), Conditions for the formation of hot flow anomalies, *J. Geophys. Res.*, 105, 12639.

Sibeck, D., N. Borodkova, G. Zastenker, S. Romanov, and J. Sauvaud (1998), Gross deformation of the dayside magnetopause, *Geophys. Res.Lett.* , 25 (4), 453.

Sibeck, D. G. , et al. (1999), Comprehensive study of the magnetospheric response to a hot ow anomaly, *J. Geophy. Res.*, 104, 4577.

Sibeck, D. G., K. Kudela, R. P. Lepping, R. Lin, Z. Nemecek, M. N. Nozdrachev, T. D. Phan, L. Prech, J. Safrankova, H. Singer, and Y. Yermolaev (2000), Magnetopause motion driven by interplanetary magneticeld variations, *J. Geophys. Res.*, 105, 25,155.

Sibeck, D. G., N. Omidi, I. Dandouras, and E. Lucek (2008), On the edge of the foreshock: model-data comparisons, Ann. Geophys., 26, 1539.

S. H. Lee, D. G. Sibeck, N. Omidi, M. V. D. Silveira, B. L. Giles, R. B. Torbert, C. T. Russell, H. Wei, J. L. Burch (2020), Comparison of MMS Observations of Foreshock Bubbles with the Global Hybrid Simulation, *J. Geophys. Res.*, submitted.

Thomas, V., et al. (1991), Hybrid simulation of the formation of a hot flow anomaly, *J. Geophys. Res.*, 96.

Thomsen, M. F., et al. (1986), Hot diamagnetic cavities upstream of the earth's bow shock, *J. Geophys. Res.*, 91, 2961.

Thomsen, M. F., et al. (1988), On the origin of hot diamagnetic cavities near the earth's bow shock, *J. Geophys. Res.*, 93, 11311.

Thomsen, M.F., et al. (1993), Observational test of hot flow anomaly formation by the interaction of a magnetic discontinuity with the bow shock, *J. Geophys. Res.*, 98, 15319.

Turner, D. L., N. Omidi, D. G. Sibeck, and V. Angelopoulos (2013), First observations of foreshock bubbles upstream of Earth's bow shock: Characteristics and comparisons to HFAs, *J. Geophys. Res. Space Physics*, 118, doi:10.1002/jgra.50198.

Turner, D., T. Liu, et al. (2020), Microscopic, multipoint characterization of foreshock bubbles with Magnetospheric Multiscale (MMS), *J. Geophys. Res. Space Physics*, in press.

Wilson III, L. B., et al. (2016), Relativistic electrons produced by foreshock disturbances observed upstream of Earth's bow shock, *Phys. Rev. Lett.*, *117*, 215101.

Zhang, H., D. G. Sibeck, Q.-G. Zong, S. P. Gary, J. P. Macfadden, D. Lason, K.-H. Glassmeier, and V. Angelopoulos (2010), Time history of events and macroscale interactions during substorms observations of a series of hot flow anomaly events, J. Geophys. Res., 115, A12235, doi:10.1029/2009JA015180.

Zhang, H., D. Sibeck, Q.G. Zong, N. Omidi, D. Turner, and L.N. Clausen (2013), Spontaneous hot flow anomalies at quasi-parallel shocks: 1. Observations, *J. Geophys.Res.*, 118,1-7, doi:10.1002/jgra.50376.

FIGURE CAPTIONS

Figure 1a-d depicts 4 configurations for FB formation and topology based on the directions of the IMF and the discontinuity normal vector (**n**). When the IMF and **n** are parallel we expect spherical foreshock bubbles to form. When IMF and **n** are perpendicular we expect planar foreshock bubbles to form.

Figure 2a-d show the density, magnetic field strength, ion temperature and ion velocity in X direction respectively from a global hybrid simulation run with radial IMF and solar wind Alfvén Mach number of 15. Panel (a) shows the shock wave, sheath and core regions of the spherical FB that forms in the run.

Figure 3a-d show the density, magnetic field strength, ion temperature and ion velocity in X direction respectively from a global hybrid simulation run with IMF cone angle of 15^o and solar wind Alfvén Mach number of 15. It is evident that compared to Figure 2, the FB in this figure is more elongated in the Y direction.

Figure 4a-d show the density, magnetic field strength, ion temperature and ion velocity in X direction respectively from a global hybrid simulation run with IMF cone angle of 30^o and solar wind Alfvén Mach number of 15. It is evident that compared to Figures 1 and 2, the FB in this figure is more elongated in the Y direction.

Figure 5a-d show the density, magnetic field strength, ion temperature and ion velocity in X direction respectively from a global hybrid simulation run with IMF cone angle of 60^o and solar wind Alfvén Mach number of 15. Formation of a planar FB is evident. Panels (e)-(h) show the time series data for ion temperature, flow velocity in X, density and magnetic field strength measure by the simulated spacecraft marked as "S" in panel (b).

Figure 6a shows the ion temperature zoomed near the bow shock and the FB for the run with IMF cone angle of 60^o and solar wind Alfvén Mach number of 15. Also shown are a couple of magnetic field lines. The presence of backstreaming ions originating from the FB shock and reaching the quasi-perpendicular bow shock is evident. Panels 6b-c show the density and ion temperature from a global hybrid simulation run with IMF cone angle of 89^o and solar wind Alfvén Mach number of 15. No foreshock bubble is formed in this case.

Figure 7a-d show the density at 4 different times during a nearly radial IMF run with RD normal (**n**) along the Y direction. Interaction of the RD represented by dashed line with the foreshock results in the formation of a planar FB while the interaction with the bow shock results in the formation of an HFA.

Figure 8 a-c show the density from 3 runs with radial IMF and solar wind Alfvén Mach numbers of 15, 11 and 7 respectively demonstrating the weakening of the FB with decreasing Mach number.

Figure 9 a-c show the density from 3 runs with IMF cone angle of 60^{o} and solar wind Alfvén Mach numbers of 15, 11 and 7 respectively demonstrating the weakening of the planar FB with decreasing Mach number.

Figure 10 a-d show the density from 4 local runs with solar wind Alfvén Mach numbers of 11, 9, 8 and 7 respectively demonstrating the weakening of the FB with decreasing Mach number.

Figure 11 a-d show the density from 4 local runs with solar wind Alfvén Mach numbers of 11 and beam densities of 5%, 2.5%, 1% and 0.5% respectively demonstrating the weakening of the FB with decreasing ion beam density.

Figure 12 a-d show the Z component of the magnetic field and total ion temperature at 4 times during a local run with ion beam density of 0.5% of solar wind where no FB is formed. Note that the RD remains relatively unchanged in time and no ions are found to reflect from the RD.

Figure 13 a-d show the Z component of the magnetic field and total ion temperature at 4 times during a local run with ion beam density of 5% of solar wind where an FB is formed. Note that the RD grows and steepens due to interaction with the ion beam and results in the reflection of a portion of these ions.

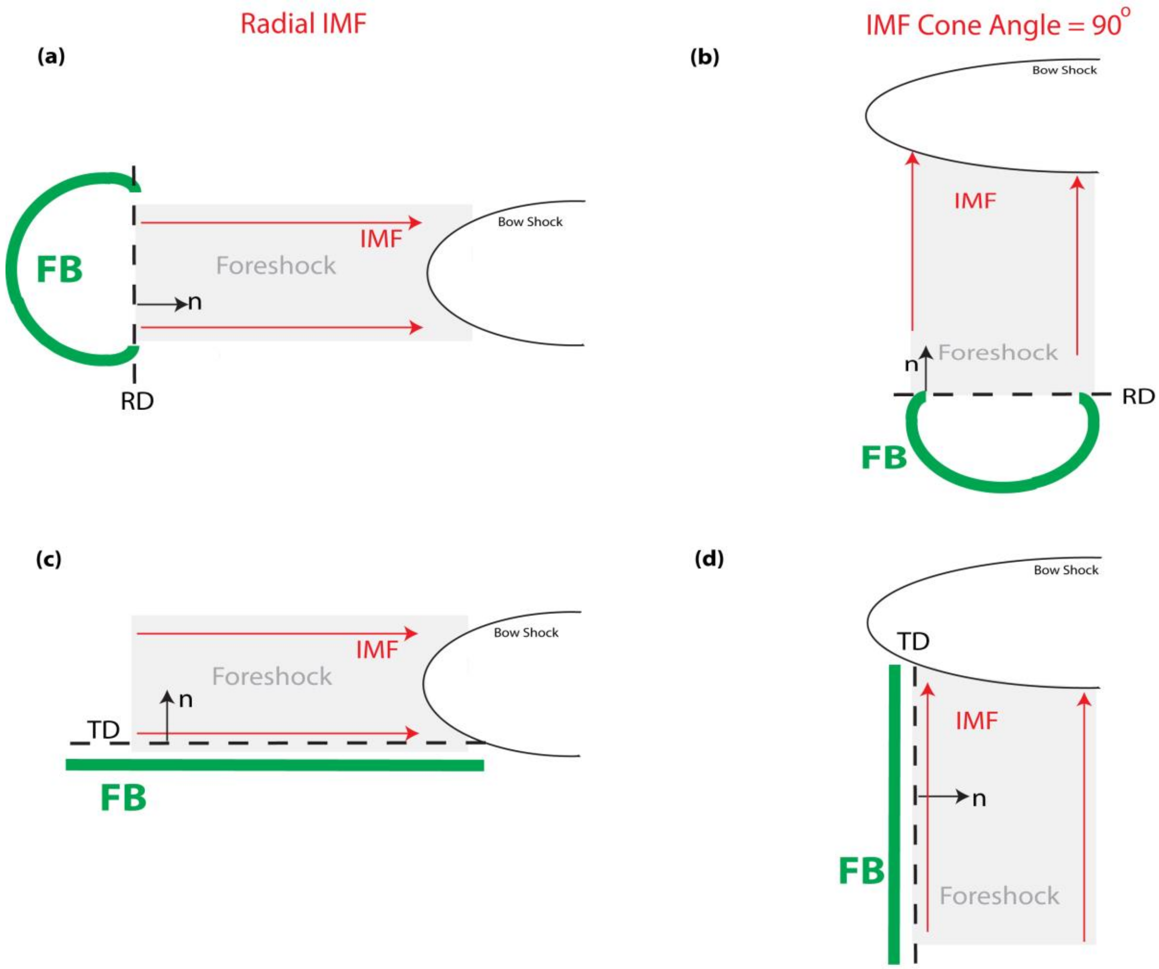

Figure 1a-d depicts 4 configurations for FB formation and topology based on the directions of the IMF and the discontinuity normal vector (**n**). When the IMF and **n** are parallel we expect spherical foreshock bubbles to form. When IMF and **n** are perpendicular we expect planar foreshock bubbles to form.

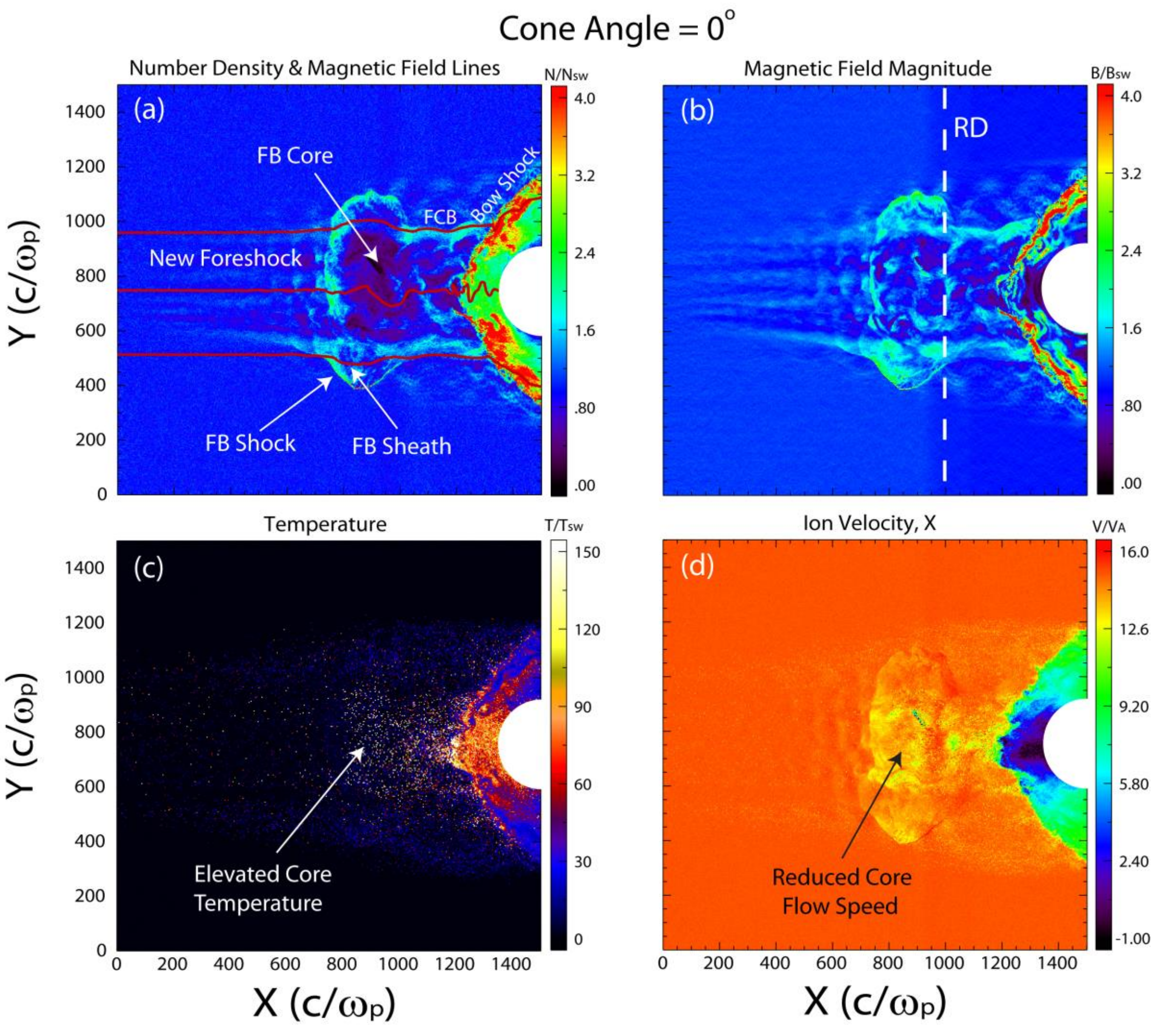

Figure 2a-d show the density, magnetic field strength, ion temperature and ion velocity in X direction respectively from a global hybrid simulation run with radial IMF and solar wind Alfvén Mach number of 15. Panel (a) shows the shock wave, sheath and core regions of the spherical FB that forms in the run.

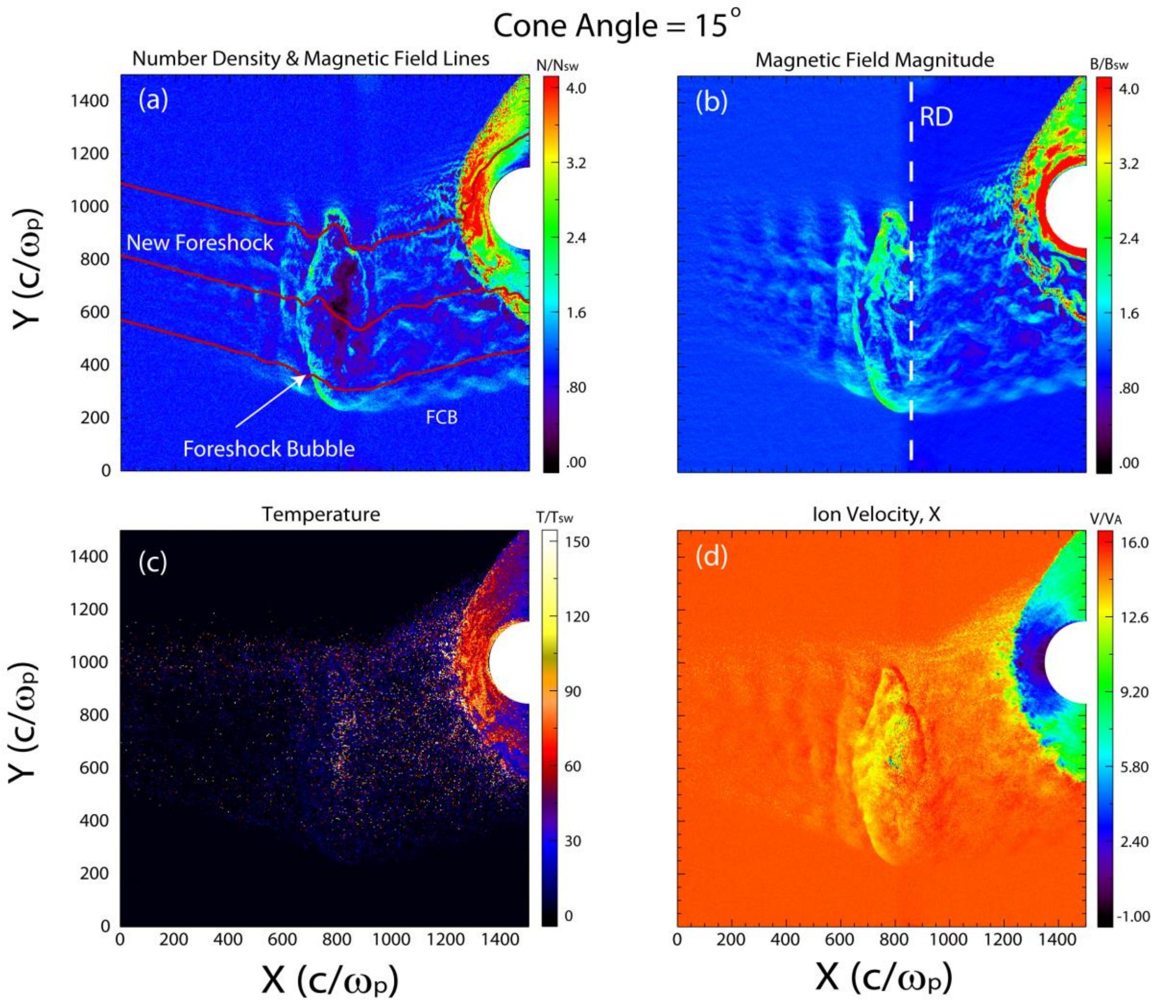

Figure 3a-d show the density, magnetic field strength, ion temperature and ion velocity in X direction respectively from a global hybrid simulation run with IMF cone angle of 15^o and solar wind Alfvén Mach number of 15. It is evident that compared to Figure 2, the FB in this figure is more elongated in the Y direction.

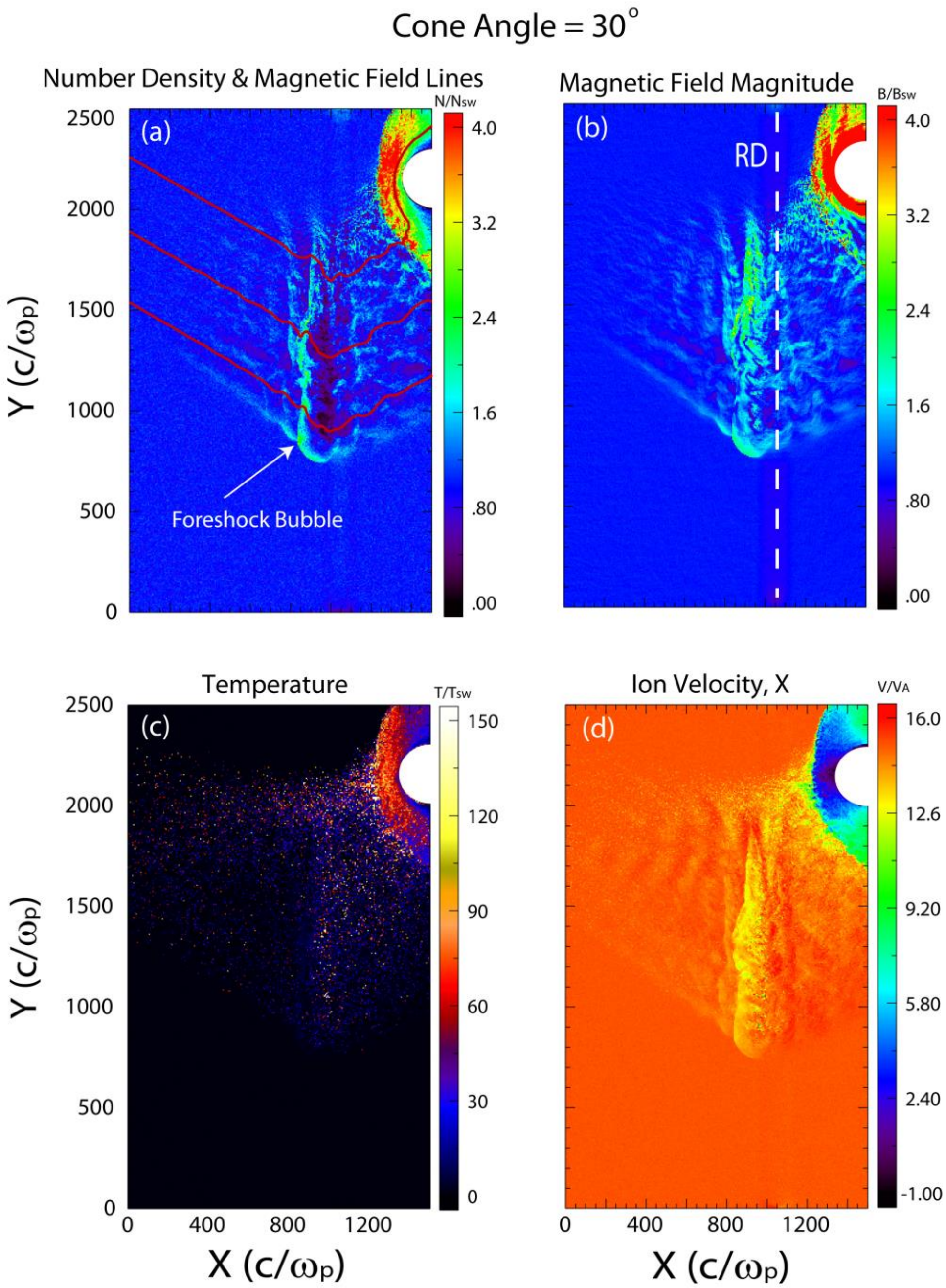

Figure 4a-d show the density, magnetic field strength, ion temperature and ion velocity in X direction respectively from a global hybrid simulation run with IMF cone angle of 30^{o} and solar wind Alfvén Mach number of 15. It is evident that compared to Figures 1 and 2, the FB in this figure is more elongated in the Y direction.

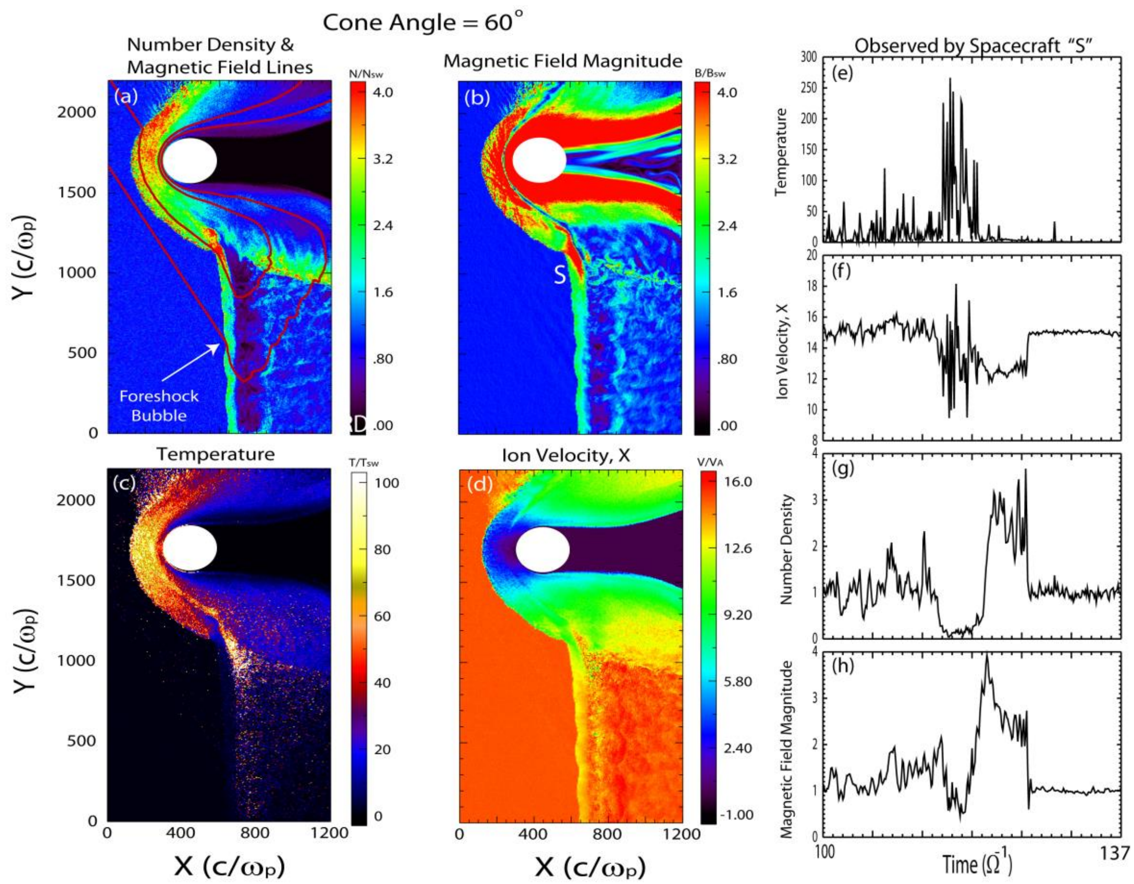

Figure 5a-d show the density, magnetic field strength, ion temperature and ion velocity in X direction respectively from a global hybrid simulation run with IMF cone angle of 60^{o} and solar wind Alfvén Mach number of 15. Formation of a planar FB is evident. Panels (e)-(h) show the time series data for ion temperature, flow velocity in X, density and magnetic field strength measure by the simulated spacecraft marked as "S" in panel (b).

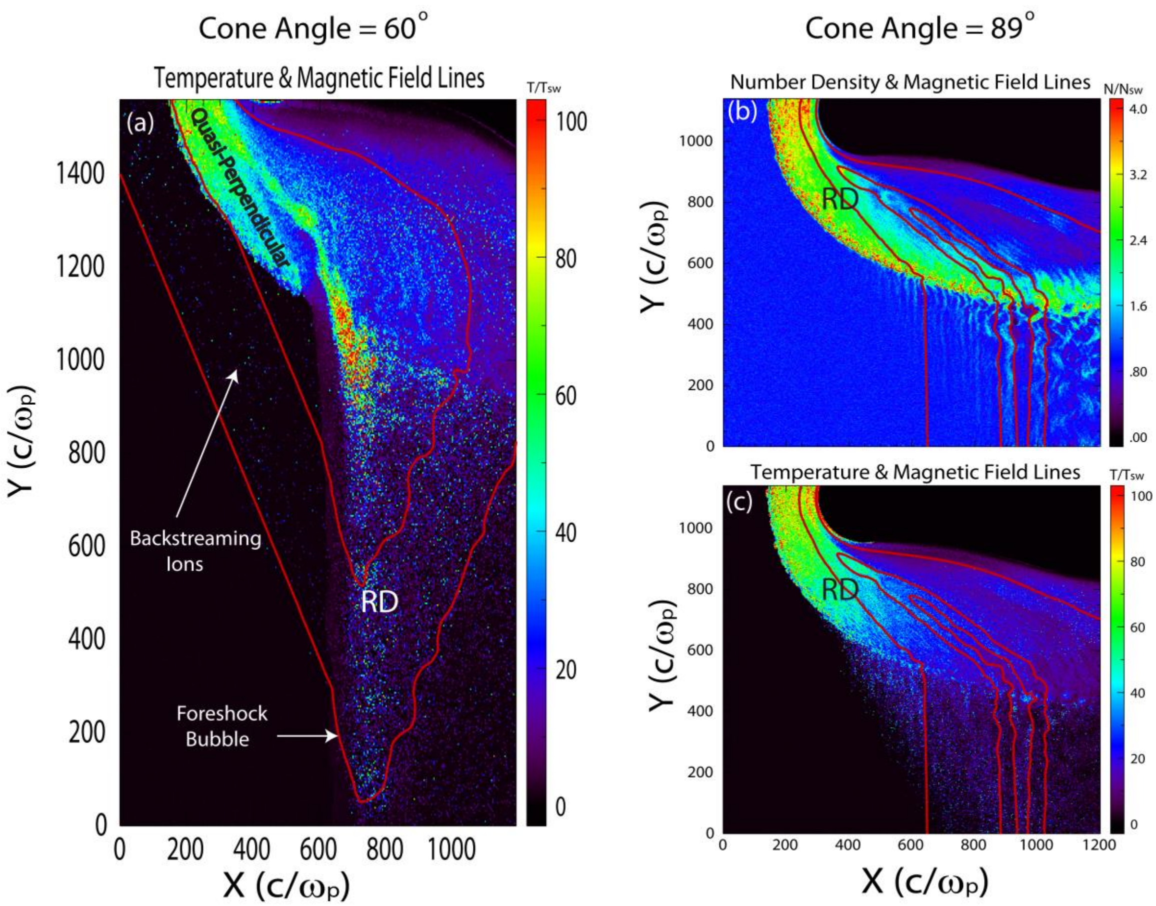

Figure 6a shows the ion temperature zoomed near the bow shock and the FB for the run with IMF cone angle of 60^o and solar wind Alfvén Mach number of 15. Also shown are a couple of magnetic field lines. The presence of backstreaming ions originating from the FB shock and reaching the quasi-perpendicular bow shock is evident. Panels 6b-c show the density and ion temperature from a global hybrid simulation run with IMF cone angle of 89^o and solar wind Alfvén Mach number of 15. No foreshock bubble is formed in this case.

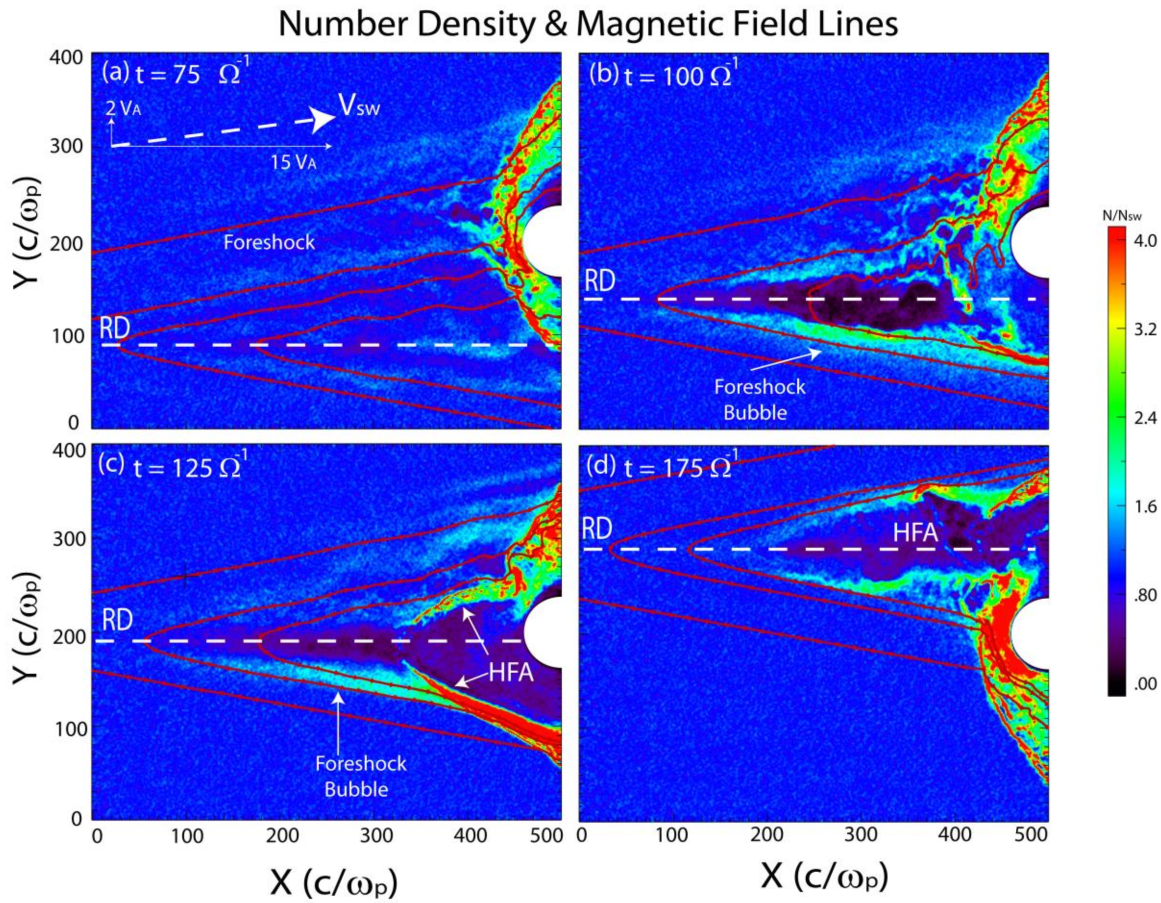

Figure 7a-d show the density at 4 different times during a nearly radial IMF run with RD normal (**n**) along the Y direction. Interaction of the RD represented by dashed line with the foreshock results in the formation of a planar FB while the interaction with the bow shock results in the formation of an HFA.

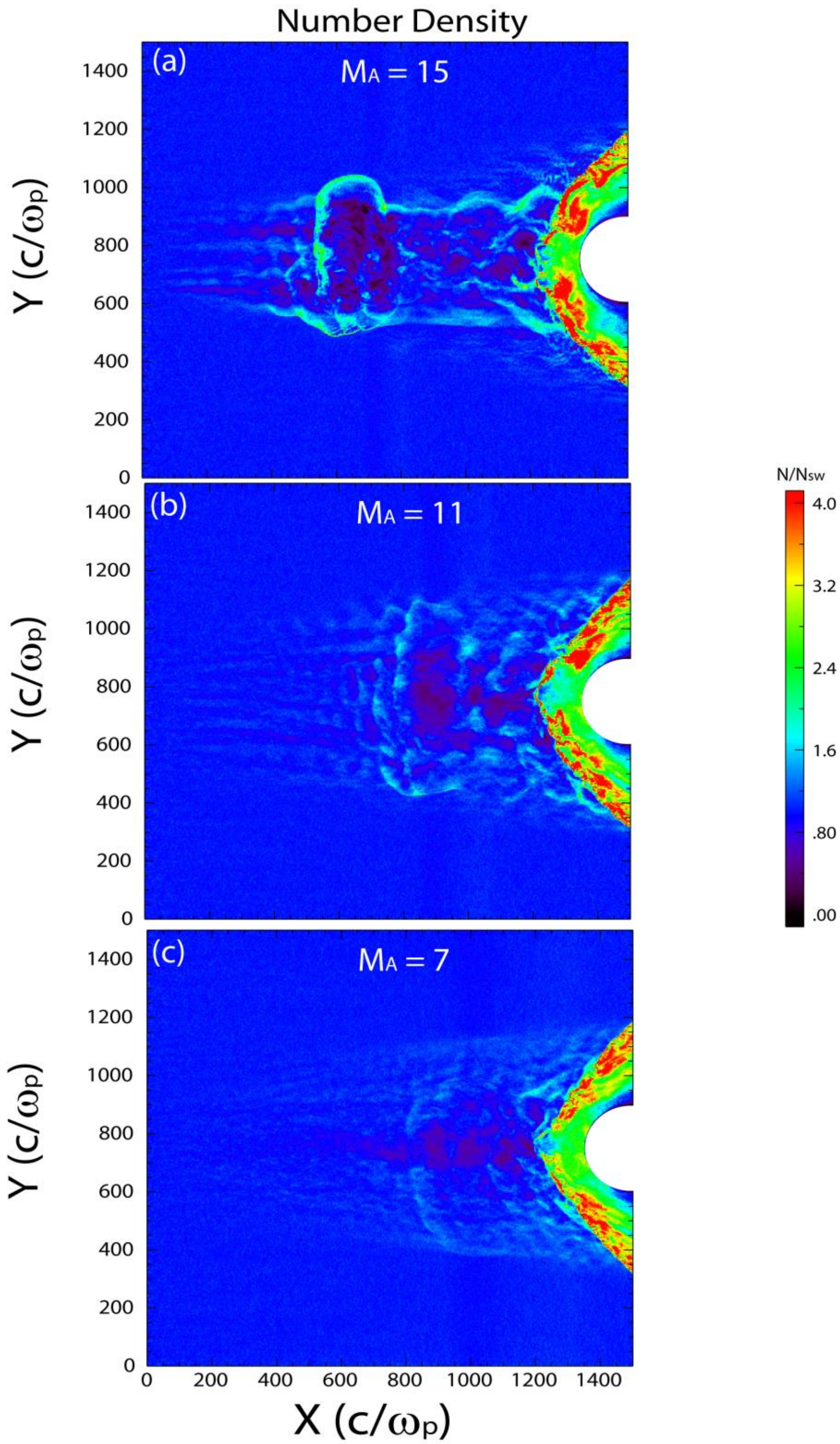

Figure 8 a-c show the density from 3 runs with radial IMF and solar wind Alfvén Mach numbers of 15, 11 and 7 respectively demonstrating the weakening of the FB with decreasing Mach number.

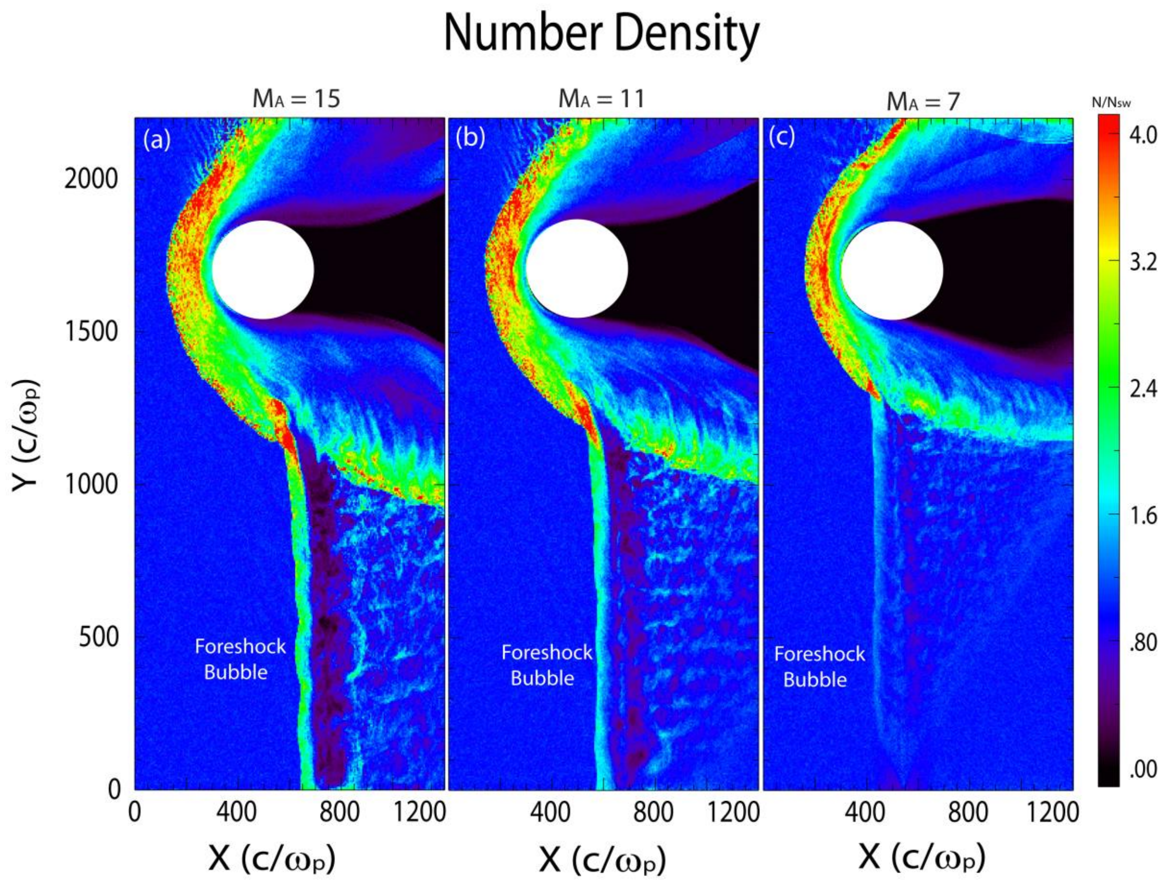

Figure 9 a-c show the density from 3 runs with IMF cone angle of 60^o and solar wind Alfvén Mach numbers of 15, 11 and 7 respectively demonstrating the weakening of the planar FB with decreasing Mach number.

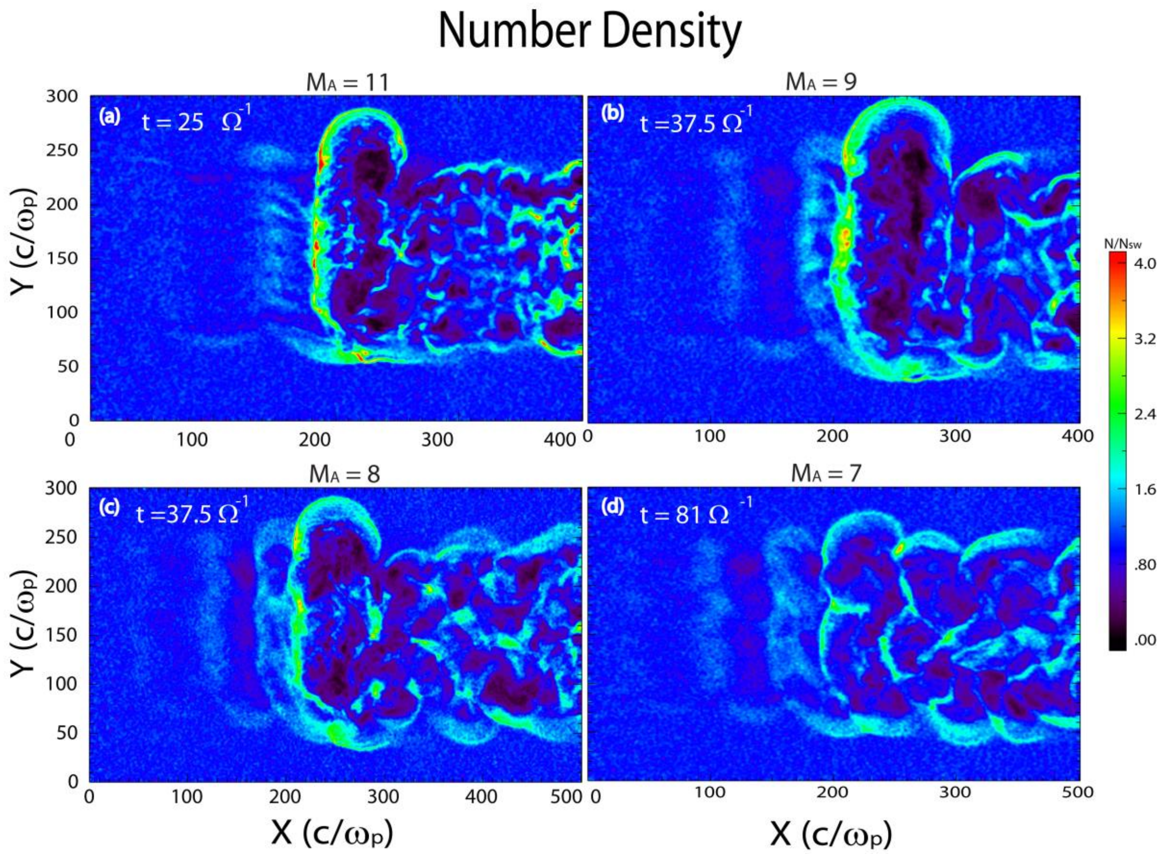

Figure 10 a-d show the density from 4 local runs with solar wind Alfvén Mach numbers of 11, 9, 8 and 7 respectively demonstrating the weakening of the FB with decreasing Mach number

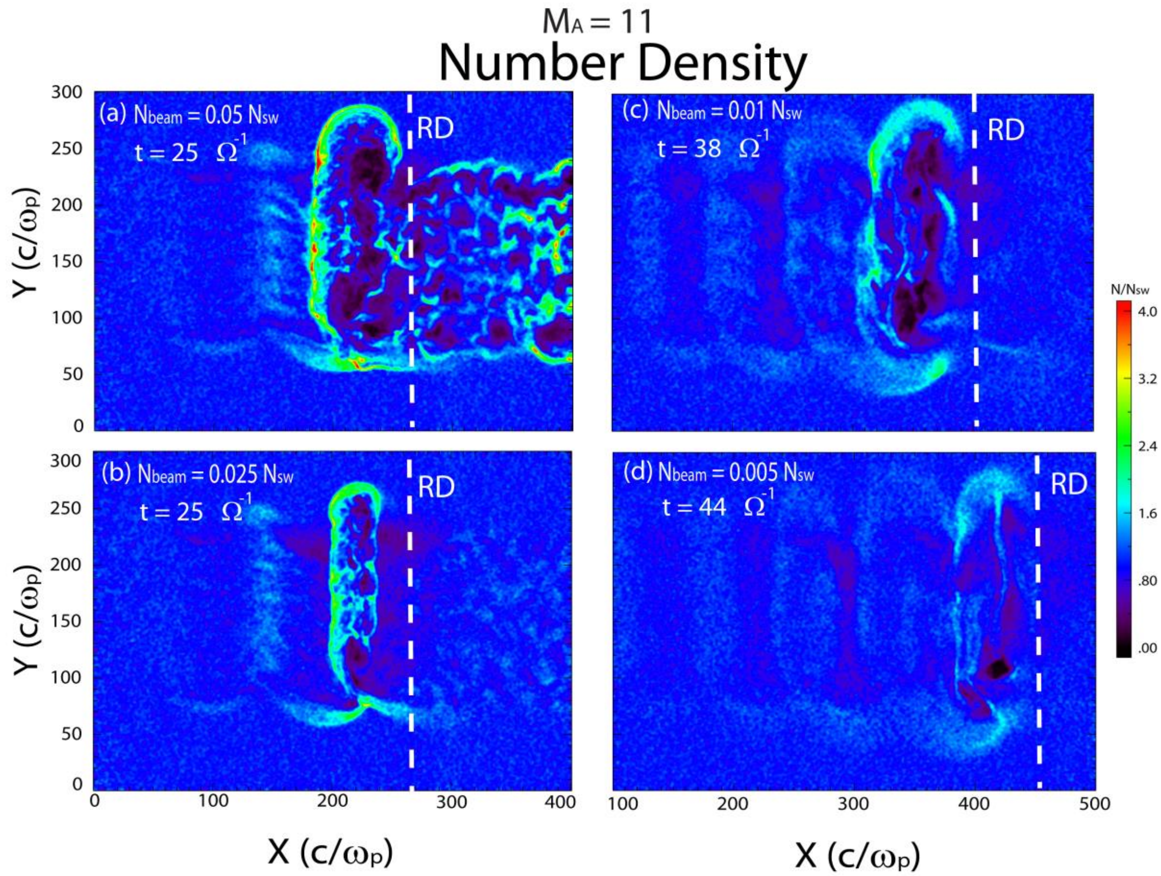

Figure 11 a-d show the density from 4 local runs with solar wind Alfvén Mach numbers of 11 and beam densities of 5%, 2.5%, 1% and 0.5% respectively demonstrating the weakening of the FB with decreasing ion beam density.

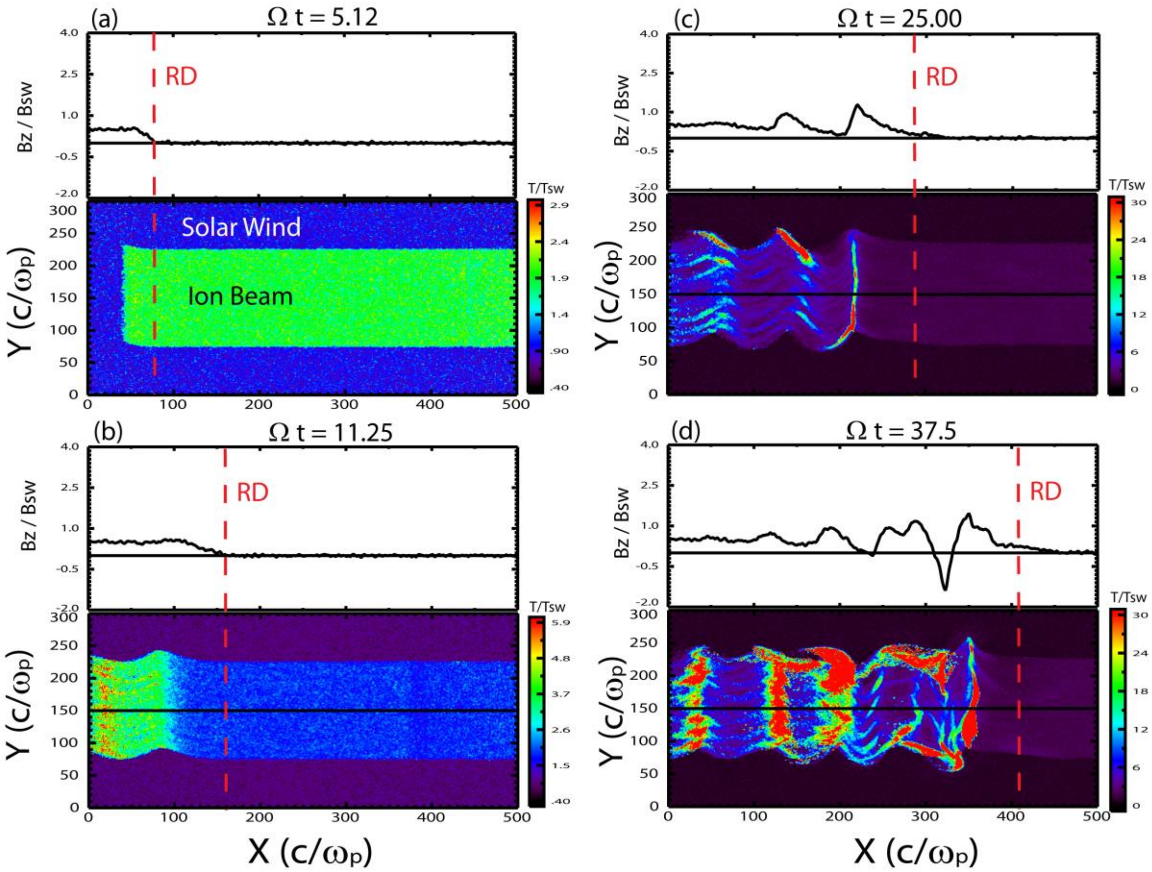

Figure 12 a-d show the Z component of the magnetic field and total ion temperature at 4 times during a local run with ion beam density of 0.5% of solar wind where no FB is formed. Note that the RD remains relatively unchanged in time and no ions are found to reflect from the RD.

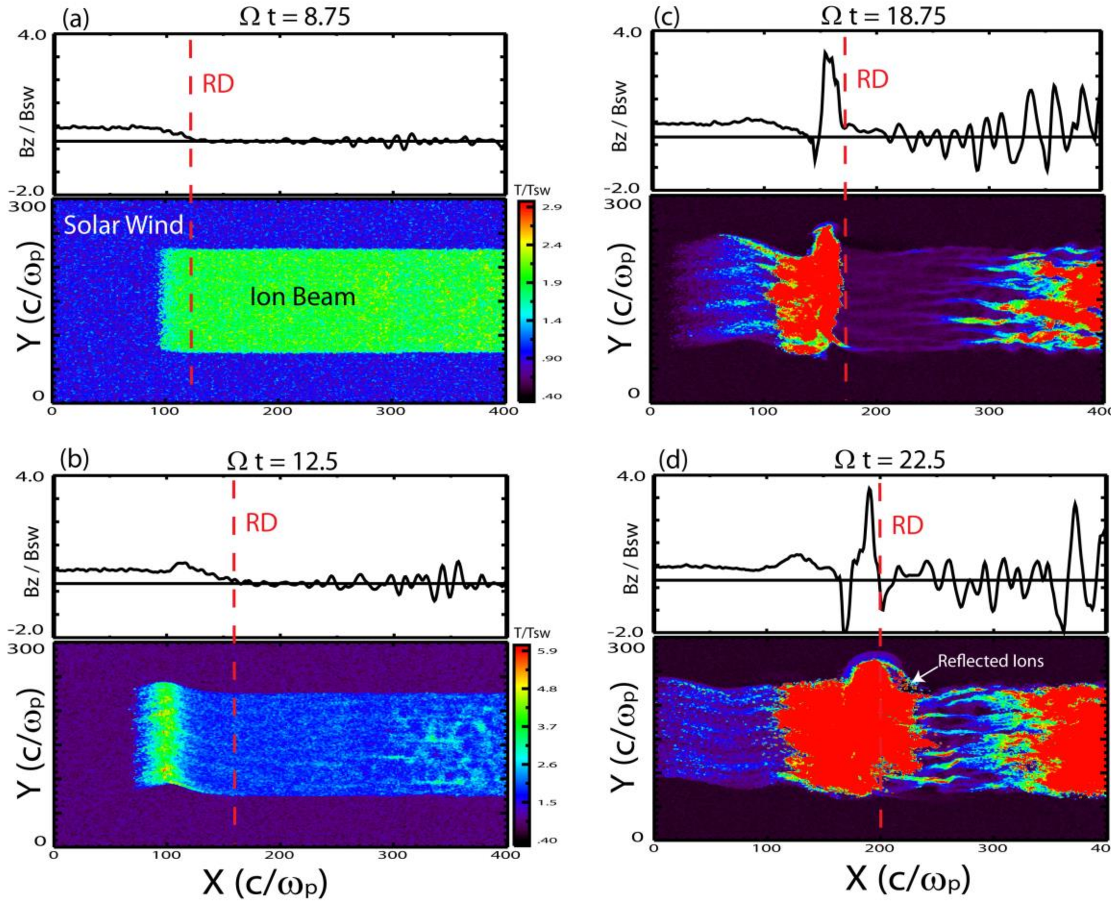

Figure 13 a-d show the Z component of the magnetic field and total ion temperature at 4 times during a local run with ion beam density of 5% of solar wind where an FB is formed. Note that the RD grows and steepens due to interaction with the ion beam and results in the reflection of a portion of these ions.